# A Biomimetic Elastic-Cable-Driven Quadruped Robot: Design, Dynamics and Controls

**Elvedin Kljuno, Ph.D., Jim Zhu, Ph.D., and Robert L. Williams II, Ph.D.**

ek289806@ohio.edu, zhuj@ohio.edu, williar4@ohio.edu

Ohio University Russ College of Engineering, Stocker Center, Athens, OH 45701

## ABSTRACT

State of the art legged robots, such as Honda's bipedal walking robot ASIMO and the bipedal robot WABIAN of Waseda University, employ joint-mount motors, which simplifies the analysis/design and allows an effective control system, but results in legs that are heavy and bulky. Cable-driven robots overcome this shortcoming by mounting the motors on the torso, thereby reducing the weight and inertia of the legs, resulting in lower overall weight and power consumption. Typical cable-driven robots use non-elastic cables; elastic cable-driven walking is explored in this article. The drive trains of conventional joint-mounted and cable-driven designs are rigid, which cannot effectively absorb ground impact shocks nor transfer potential energy to kinetic energy and vice versa when the robot is in motion, as biological animals do.

In this article we present the design and testing of a cat-size quadruped robot called RoboCat, which employs stretchable elastic cable-driven joints as inspired by biological quadrupeds. Although it complicates kinematics and dynamics analysis and design, the elastic cables and torso-mounted motors enable weight and power savings relative to conventional designs. The elastic cable-driven joints not only absorb ground contact shock, but also transfer potential and kinetic energy during walking or running, thereby improving the robot motion performance and energy efficiency. In this article we discuss the kinematics and dynamics analysis of elastic cable-driven joints, implementation of elastic cable-driven joints on the Ohio University RoboCat, and control.

## 1. INTRODUCTION

Traditional direct-drive robotic actuation systems are one of the easiest ways to actuate walking robot, due to mechanical simplicity and the fact that the motors rotation is directly mapped into joints rotation. For basic robot walking functionality, direct drives with a gear set would be a convenient solution. However, biological walkers that use an inverted-pendulum-like mechanism [1–3] are considered energy-efficient relative to the state of the art walking robots [4,5]. Biological walkers use a different kind of actuators, the muscles, which can be considered as elastic linear actuators. Energy efficiency and walk cycle precision and smoothness are among the important reasons for mimicking biological walkers. Muscle behavior and structure attract special attention in robotics research. There have been a number of attempts to produce artificial muscles for use in robotics [6–10], based on different principles such as pneumatics, piezoelectric effect, and magnetostriction.

One possibility for walking robot muscle-like actuation is to use elastic cables. Applications of cable actuation in general robotics [11] show that cable actuation can achieve relatively high accelerations, due to the reduced mass of the most kinetically-active robot segments.

Since walking robots usually have to carry an independent energy source (batteries), it is critical to reduce the energy consumed per distance. Using cables the motors are moved to the sections of the robot that are the least kinetically-active and experience the lowest accelerations. The main benefits are: balancing stability of the robot is improved and the energy consumption is reduced due to the reduced mass of the fast moving segments of the walking robot. It will also lead to significantly reduced overall weight of the robot. There are other benefits not directly included in this article scope.

Some work has been done in the area of cable actuation for walking robotics. A partially-cable-actuated hexapod is analyzed in [12].

The current article presents a novel development of kinematics, dynamics, and control for elastic-cable-driven walking robots. Section 2 presents kinematic and dynamics analysis of a quadruped walking robot and Section 3 presents a novel controller for this, with simulated results and discussion.

## 2. KINEMATICS AND DYNAMICS ANALYSIS OF THE QUADRUPED WALKING ROBOT

### 2.1 The Walking Robot Architecture

The walking robot architecture under consideration is shown in Figure 1a. The robot architecture has 4 actuated dof (hip, knee, ankle, pulley) for each leg corresponding to the longitudinal motion and additional 2-dof (hip and ankle) for each leg corresponding to the lateral motion. The actuated revolute joints are marked by R in Figure 1a.

The RoboCat design considered here is the result of partial biomimicry with significant reduction in dof. The trunk segment does not contain flexibility, while a biological cat has significant flexibility in the trunk, which simplifies a locomotion direction change. The robot architecture still enables the locomotion change through the inclusion of the two (per leg) revolute antero-posterior-oriented joints at the hip and at the ankle. Other revolute joints (hip, knee, and ankle) connecting the leg segments provide the motion parallel to the sagittal (symmetry) plane. The initial hardware developed is shown in Figure 1b.

The cables for knee joint actuation are pulled using specially shaped pulleys on the trunk. This design detail deviates from the biological case and has a significant disadvantage in that the cable forces can produce significant coupling between the knee and the hip joint, since the cables for the knee can generate significant torque for the hip, if controlled for.

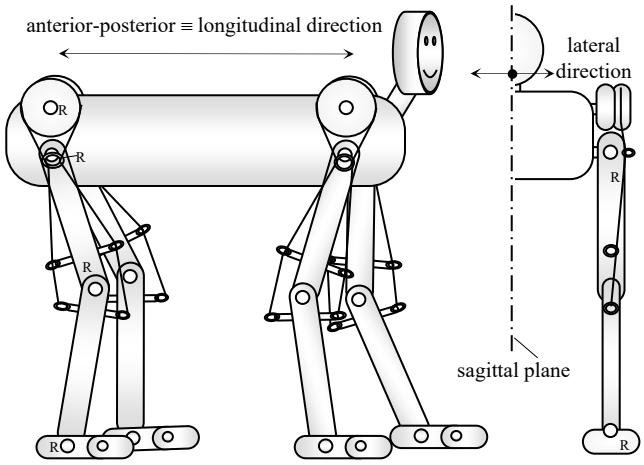


**Figure 1a. The RoboCat architecture**

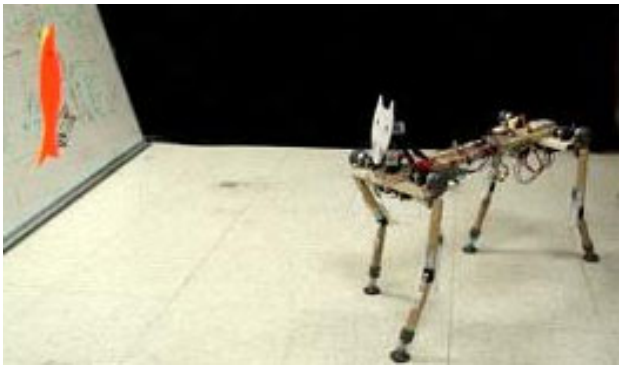

**Figure 1b. The RoboCat Hardware**

The length and the position of the bars with the cable attachment points about the knee joint directly influence the required variable cable tension over the joint motion range, as well as the variable cable pulling speed. Further, the required cable tension and speed to calculate power are required for motor sizing. Also the gear ratio selection directly depends on the pulley size and shape.

A biological hip joint is a 3-dof spherical joint, but it is difficult to design a direct-drive actuation system for a robotic hip joint. However, using cables, the option of using spherical joints is recommended, since it reduces the number of cables needed (4 cables for a spherical joint) comparing with separate three revolute joints (6 cables for three separate 1-dof joints). For the sake of simplicity, we decided to consider that only the knee joint is actuated using cables.

The architecture is presented without specifying details. The proper sizing and detailed design specifications need to be done iteratively using a mathematical model of the system.

**2.2 Mathematical Modeling Parameters and Assumptions**

The significant assumptions for mathematical model derivation are:

1) The contact surfaces between cables and guiding holes are frictionless,
2) The cables are ideally flexible, i.e. bending moments are zero,
3) The elastic cables behave as linear springs,
4) The lateral motion does not produce significant inertial effects on the longitudinal motion,
5) Walking is performed on a horizontal flat plane,
6) The robot system walking is statically stable.

The walking cycle for a leg consists of two main phases: the support phase and the swing phase. Since the dynamics of a stance leg with the trunk is significantly different from the dynamics of a swing leg alone, we can model them separately and combine them in the quadruped model via interconnection forces and torques. Alternatively we can model them together, increasing the mathematical model complexity. A simplified stance leg model with a concentrated mass of the trunk is shown in [13], which represents a compact model convenient for model-based control due to relatively low computational load. The model of the quadruped in [13] considers dynamics of each leg separately and then it combines them via interconnection forces and moments. In contrast to that model, here we consider the stance leg, swing leg and the trunk together, which increases the complexity of the model, but has a potential to give better results for better controller performance. The stance and swing leg with the trunk model is shown in Figure 2.

The influence of the other legs on the trunk is represented through the horizontal and the vertical component of the interaction force relocated to the trunk CG ($C_t$), along with the torque resulting from the reallocation of the forces.

The dynamics of this system is governed by several parameters that are now discussed in subsections below.

**Cable stiffness.** One of the most important parameters is the cable spring stiffness. The physical quantity in animals that corresponds to the stiffness of the cables is the effective stiffness of the muscles and tendons. Tendons accumulate a portion of energy that would be normally lost due to a foot-ground collision. The accumulated energy is released during the next gait cycle to decrease the amount of the kinetic energy input via the muscles. A similar effect is expected using the elastically stretchable cables for the walking robot. The contact forces and joint torques are expected to smooth out, which is desirable in robot control. However, a potential problem using elastic cables is that the system can experience an oscillating behavior without sufficient damping, which requires a dynamic controller to stabilize the system.

**Cable attachment Points.** The points where the cables are attached relative to the joints and the cable guidance geometry are important. The points where the cable guiding holes are positioned (A, A', B and B' in Figure 2) determine the joint axis moment arm, along with the joint angular motion range. Inappropriate position of the guiding holes can result in a high cable tension required to generate required torques at specific joint angles. Therefore, good positions of the guiding rings and the attachment points will be determined via numerical solutions and simulations.

**Pulleys profile.** The pulleys are designed to have a variable radius profile, as shown in Figure 3.

The objective of the variable pulley radius is to compensate for the difference in the cable length increase on one side and the cable length decrease on the other side of the knee joint. Considering the architecture shown in Figure 2, the cable length increase between points B and B' is not the same as the cable length decrease between points A and A', as shown in Figure 4. This causes problems if the variation of the sum $\overline{AA'}+\overline{BB'}=f(\varphi_2)$ is significant, since a pulley with constant radius would release the same cable length as the cable length that it stores for the same angle of rotation. This difference can be compensated to a certain extent with preloaded springs attached in series along the cables. However, experiments showed that the spring stiffness must be significantly decreased to compensate large variation of $\overline{AA}(\varphi_2)+\overline{BB}(\varphi_2)$, which will reduce the effective torques it can

provide to the joints. The variable radius pulley is an effective solution to enable a single motor to drive elastic cables. The design objective is that if the cable were not stretched, the pulley angle of rotation should be proportional to the rotation of the knee joint, that is

$$\frac{\varphi_2}{\varphi_4} = k = \text{constant}\,.$$

The constant $k$ is a modeling parameter that influences the controller sensitivity and performance; it will be considered in simulation results.

Clearly, there is no need for the variable radius pulley in the case when two motors are used to pull the two cables separately. However, the intention here is to use only one motor to drive a revolute joint. The mathematical model derivation requires detailed kinematic analysis, discussed next.

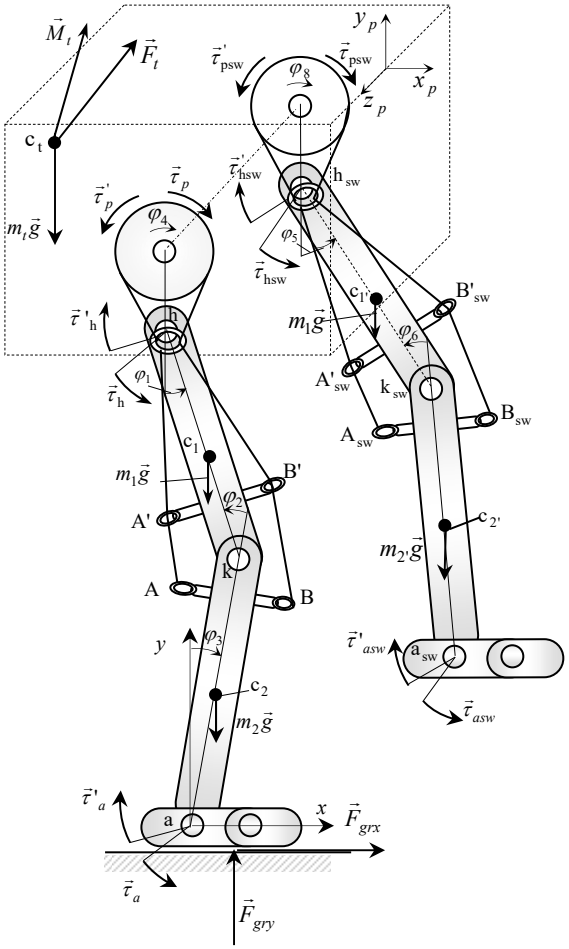


**Figure 2. The Stance and Swing leg model**

### 2.3 Kinematics

The objective of kinematics analysis of the walking robot, actuated by elastic cables, is to find the relationships between the joint angles and the Cartesian positions in an inertial coordinate system, as well as the corresponding velocities. The kinematic analysis also needs to provide the relationship between cable speed and angular speed of the joint. In this particular case, the aforementioned relationship represents the relationship between the pulley angular speed and the knee joint angular speed for the case when there is no change in the cable length. The cables are stretched and are assumed to behave as preloaded linear springs, deformation and kinematics are coupled with the dynamics through the deformation and forces of the springs.

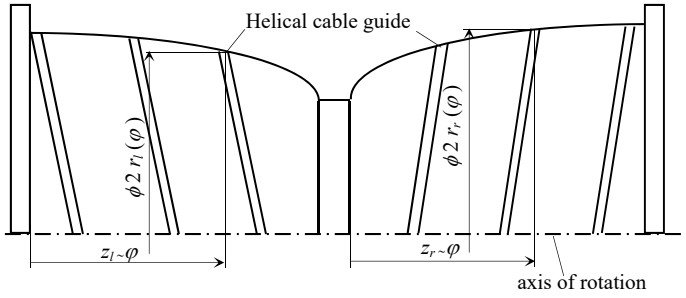


**Figure 3. The pulley profile**

Expressing the velocities of the CGs in the ground attached inertial coordinate frame requires expressions of the Cartesian coordinates in terms of the joint angles, which are obtained as follows.

$$\vec{r}_{C1} = \begin{bmatrix} l_2 s\varphi_3 - l_{C1} s\varphi_{23} \\ l_2 c\varphi_3 + l_{C1} c\varphi_{23} \end{bmatrix} \qquad \vec{r}_{C1'} = \begin{bmatrix} l_2 s\varphi_3 - l_1 s\varphi_{23} - l_{c1'} s\varphi_{1235} \\ l_2 c\varphi_3 + l_1 c\varphi_{23} - l_{c1'} c\varphi_{1235} \end{bmatrix}$$

$$\vec{r}_T = \begin{bmatrix} l_2 s\varphi_3 - l_1 s\varphi_{23} + l_{t1} s\varphi_{123} + l_{t2} c\varphi_{123} \\ l_2 c\varphi_3 + l_1 c\varphi_{23} + l_{t1} c\varphi_{123} - l_{t2} s\varphi_{123} \end{bmatrix} \qquad \vec{r}_{C2} = \begin{bmatrix} l_{C2} s\varphi_3 \\ l_{C2} c\varphi_3 \end{bmatrix}$$

$$\vec{r}_{C2'} = \begin{bmatrix} l_2 s\varphi_3 - l_1 s\varphi_{23} - l_1 s\varphi_{1235} - l_{c2'} s\varphi_{12356} \\ l_2 c\varphi_3 + l_1 c\varphi_{23} - l_1 c\varphi_{1235} - l_{c2'} c\varphi_{12356} \end{bmatrix} \qquad (1)$$

where $l_{Ci}$, $(i = 1, 2)$ are the lower parts of the leg segments lengths from the joints to the CGs, $l_{C1'} = l_1 - l_{C1}$ , $l_{C2'}$ represents the distance from the knee joint to the CG of the swing leg lower part including the foot lumped mass, $l_{t1}$ and $l_{t2}$ are the $x_p$ and $y_p$ coordinates of the trunk CG ($c_t$) with respect to the hip joint (i.e. the components of $\overrightarrow{hc_t}$ ); the angles with indices are defined as:

$\varphi_{ij} = \varphi_i - \varphi_j$ , $\varphi_{ijk} = \varphi_i - \varphi_j + \varphi_k$ , $\varphi_{ijkn} = \varphi_i - \varphi_j + \varphi_k - \varphi_n$ , and
$\varphi_{ijknm} = \varphi_i - \varphi_j + \varphi_k - \varphi_n + \varphi_m$ , $(i, j, k, n, m = 1,...,6,8)$,

These angles are indicated in Figure 2. The abbreviation for sine and cosine functions are $s\psi = \sin\psi$ , $c\psi = \cos\psi$ , with $\psi$ denoting any angle. By differentiating (1) we obtain the velocities:

$$\vec{v}_{C2} = l_{C2}\dot{\varphi}_3 \begin{bmatrix} c\varphi_3 \\ -s\varphi_3 \end{bmatrix} \qquad \vec{v}_{C1} = \begin{bmatrix} l_2 c\varphi_3\dot{\varphi}_3 - l_{C1} c\varphi_{23}\dot{\varphi}_{23} \\ -l_2 s\varphi_3\dot{\varphi}_3 - l_{C1} s\varphi_{23}\dot{\varphi}_{23} \end{bmatrix}$$

$$\vec{v}_T = \begin{bmatrix} l_2 c\varphi_3\dot{\varphi}_3 - l_1 c\varphi_{23}\dot{\varphi}_{23} + l_{t1} c\varphi_{123}\dot{\varphi}_{123} - l_{t2} s\varphi_{123}\dot{\varphi}_{123} \\ -l_2 s\varphi_3\dot{\varphi}_3 - l_1 s\varphi_{23}\dot{\varphi}_{23} - l_{t1} s\varphi_{123}\dot{\varphi}_{123} - l_{t2} c\varphi_{123}\dot{\varphi}_{123} \end{bmatrix} \qquad (2)$$

$$\vec{v}_{C1'} = \begin{bmatrix} l_2 c\varphi_3\dot{\varphi}_3 - l_1 c\varphi_{23}\dot{\varphi}_{23} - l_{C1'} c\varphi_{1235}\dot{\varphi}_{1235} \\ -l_2 s\varphi_3\dot{\varphi}_3 - l_{C1} s\varphi_{23}\dot{\varphi}_{23} + l_{C1'} s\varphi_{1235}\dot{\varphi}_{1235} \end{bmatrix}$$

$$\vec{v}_{C2'} = \begin{bmatrix} l_2 c\varphi_3\dot{\varphi}_3 - l_1 c\varphi_{23}\dot{\varphi}_{23} - l_1 c\varphi_{1235}\dot{\varphi}_{1235} - l_{C2'} s\varphi_{12356}\dot{\varphi}_{12356} \\ -l_2 s\varphi_3\dot{\varphi}_3 - l_{C1} s\varphi_{23}\dot{\varphi}_{23} + l_1 s\varphi_{1235}\dot{\varphi}_{1235} - l_{C2'} c\varphi_{12356}\dot{\varphi}_{12356} \end{bmatrix}$$

Besides the relationships (1) and (2), we need an appropriate function that indicates how much and with which rate the cable should be pulled to obtain a desired joint angle and angular speed. The cable length change on the two sides of the pulley in Figure 3 is due to the change in the joint angle and to the change in the cable tension. The cable length change rates due to the knee angles change $\varphi_2$ and $\varphi_6$ are:

$$\frac{\partial}{\partial\varphi_2}l_r(\varphi_2,S_r)\dot{\varphi}_2=\frac{d}{d\varphi_2}\overline{BB'}(\varphi_2)\dot{\varphi}_2=\frac{h_{BBs}c\varphi_2-h_{BBc}s\varphi_2}{\overline{BB'}(\varphi_2)}\dot{\varphi}_2$$
$$\frac{\partial}{\partial\varphi_2}l_l(\varphi_2,S_l)\dot{\varphi}_2=\frac{d}{d\varphi_2}\overline{AA'}(\varphi_2)\dot{\varphi}_2=\frac{-h_{AAs}c\varphi_2-h_{AAc}s\varphi_2}{\overline{AA'}(\varphi_2)}\dot{\varphi}_2 \qquad (3)$$
$$\frac{\partial}{\partial\varphi_6}l_{rsw}(\varphi_6,S_{rsw})\dot{\varphi}_6=\frac{d}{d\varphi_6}\overline{BB'}_{sw}(\varphi_6)\dot{\varphi}_6=\frac{h_{BBs}c\varphi_6-h_{BBc}s\varphi_6}{\overline{BB'}_{sw}(\varphi_6)}\dot{\varphi}_6$$
$$\frac{\partial}{\partial\varphi_6}l_{lsw}(\varphi_6,S_{lsw})\dot{\varphi}_6=\frac{d}{d\varphi_6}\overline{AA'}_{sw}(\varphi_6)\dot{\varphi}_6=\frac{-h_{AAs}c\varphi_6-h_{AAc}s\varphi_6}{\overline{AA'}_{sw}(\varphi_6)}\dot{\varphi}_6$$

where $l_r$ and $l_l$ are the cable lengths on the right and on the left of the stance leg pulley, respectively, $S_r$ and $S_l$ are the cable tensions, and the quantities with "sw" in the notation are for the swing leg. In the combined geometrical parameters:

$$h_{BBs}=h_{1r}h_3+h_2h_{4r} \qquad h_{BBc}=-h_2h_3+h_{1r}h_{4r}$$
$$h_{AAs}=h_{1l}h_3+h_2h_{4l} \qquad h_{AAc}=-h_2h_3+h_{1l}h_{4l}$$

$h_{1r}$, $h_{1l}$, $h_2$, $h_3$, $h_{4r}$, $h_{4l}$ denote the position (with $h_5$ negligible) of the cable attachment points relative to the knee joint, as shown in Figures 4a and 4b.

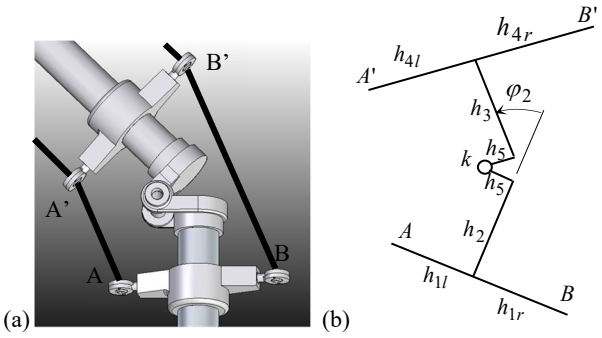


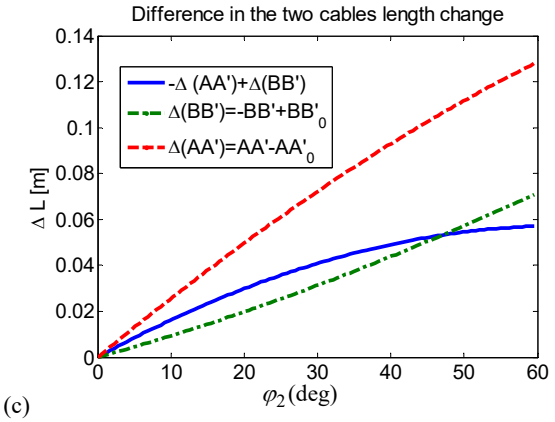


**Figure 4. (a) Cable attachment design, (b) The cable attachment points parameters, (c) Cable length change difference**

The total cable length changes on the two sides of the pulley are:

$$\Delta l_r(\varphi_2,S_r)=(S_r-S_{r0})\frac{1}{k_{sr}}+\overline{BB'}(\varphi_2)-\overline{BB'}(0)$$
$$\Delta l_l(\varphi_2,S_l)=(S_l-S_{l0})\frac{1}{k_{sl}}+\overline{AA'}(\varphi_2)-\overline{AA'}(0) \qquad (4)$$
$$\Delta l_{rsw}(\varphi_6,S_{rsw})=(S_{rsw}-S_{r0})\frac{1}{k_{sr}}+\overline{BB'}_{\mathrm{sw}}(\varphi_6)-\overline{BB'}(0)$$
$$\Delta l_{lsw}(\varphi_6,S_{lsw})=(S_{lsw}-S_{l0})\frac{1}{k_{sl}}+\overline{AA'}_{\mathrm{sw}}(\varphi_6)-\overline{AA'}(0)$$

where $k_{sr}$, $k_{sl}$ are the cable spring stiffness coefficients for the right and left cable segments.

We need to determine the pulley profile function that will provide proportional rotations of the knee joint and the pulley, for an approximately constant cable tension. The general profile of the pulley is shown in Figure 3, which indicates two rigidly joined segments corresponding to the right and left cables. The objective of this design is to reduce normally large spring deformations due to the geometrical joint angle changes.

To compensate the necessary difference in the cable stored on and released from the pulley (Figure 4c), the radius functions $r_r(\varphi_4)$ and $r_l(\varphi_4)$ must cancel the nonlinearity in $\overline{\mathrm{AA'}}(\varphi_2)$ and $\overline{\mathrm{BB'}}(\varphi_2)$. The two functions are:

$$r_s(\phi_4)=\begin{cases}R_{\min}, & \text{for } \pm\dfrac{d\overline{\mathrm{PP'}}(\phi_2)}{d\phi_2}\Big|_{\phi_2=k\phi_4}\left(\dfrac{\delta\phi_2}{\delta\phi_4}\right)_{\mathrm{des}}<R_{\min}\\ R_{\max}, & \text{for } \pm\dfrac{d\overline{\mathrm{PP'}}(\phi_2)}{d\phi_2}\Big|_{\phi_2=k\phi_4}\left(\dfrac{\delta\phi_2}{\delta\phi_4}\right)_{\mathrm{des}}>R_{\max}\\ \pm\dfrac{d\overline{\mathrm{PP'}}(\phi_2)}{d\phi_2}\Big|_{\phi_2=k\phi_4}\left(\dfrac{\delta\phi_2}{\delta\phi_4}\right)_{\mathrm{des}} & \text{otherwise}\end{cases} \qquad (6)$$

where $\left(\dfrac{\delta\varphi_2}{\delta\varphi_4}\right)_{\mathrm{des}}=k$ is the desired ratio of the two rotations, $R_{\min}$ and $R_{\max}$ are the positive minimum and maximum radii of the pulley and the derivatives are given in (3), with the plus sign for *s*=*r* and *P*=*B*. The ratio cannot be exactly constant since the cable is elastic. We cannot compensate a general cable tension force, since it is not only a function of angles, but also depends on the inertial forces and payload.

For the following parameters: $h_{1r}=h_{1l}=h_2=h_3=0.1$ m, $h_{4r}=h_{4l}=0.1$m, $k$=0.5, the radii functions of the two pulley segments are:

$$r_s(\phi_4)=\begin{cases}R_{\min}, & \text{for } 0.05\dfrac{\cos(0.5\phi_4)}{\sqrt{1\pm\sin(0.5\phi_4)}}<R_{\min}\\ R_{\max}, & \text{for } 0.05\dfrac{\cos(0.5\phi_4)}{\sqrt{1\pm\sin(0.5\phi_4)}}>R_{\max}\\ 0.05\dfrac{\cos(0.5\phi_4)}{\sqrt{1\pm\sin(0.5\phi_4)}} & \text{otherwise}\end{cases}$$

(in meters), where the plus sign is for *s*=*r*.

The profile plot for the set of parameters is shown in Figure 5. The pulley profile consists of the two sections corresponding to the back and the front cable of the knee drive unit. The derivation of the pulley assumes that the knee joint design (such as shown in Figure 4a) restricts hyperextensions, which means that the angle $\varphi_2$ has only positive values for the back legs and only negative values for the front legs of the RoboCat. We can see that two radii have the same value only for $\varphi_2=0$, when this symmetry exists.

The Lagrange energy method that we will use for the dynamics model derivation requires the CG velocities, but not the accelerations. Now, we will use the kinematics expressions to derive the walking robot dynamics model.

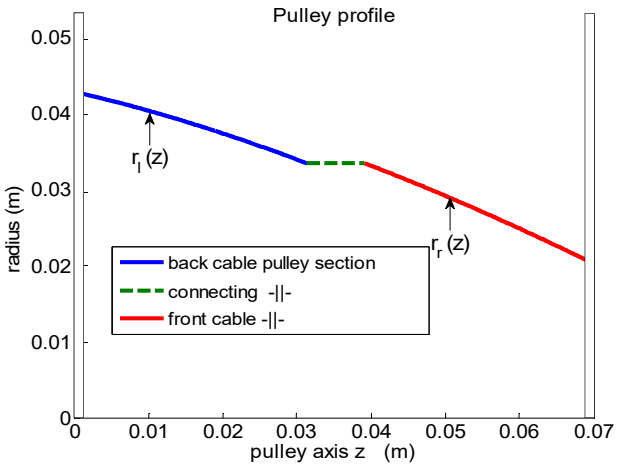


**Figure 5. The pulley profile**

### 2.4 Dynamics of the RoboCat

Using the Lagrange energy method, a set of nonlinear differential equations of second order is derived. Since the derivation details would take significant space, we will include the final results for each dof. The dynamics of the system can be represented by the matrix equation:

$$\left[\mathrm{M}(\vec{\varphi}(t))\right]\ddot{\vec{\varphi}}(t)+\left[\mathrm{C}(\vec{\varphi}(t),\dot{\vec{\varphi}}(t))\right]\dot{\vec{\varphi}}(t)+\left[\mathrm{P}(\vec{\varphi}(t))\right]=\vec{\tau}(t) \tag{7}$$

where $\vec{\varphi}(t)$, $\dot{\vec{\varphi}}(t)$ and $\ddot{\vec{\varphi}}(t)$ are the joint angle, velocity and acceleration vectors, respectively, $\left[\mathrm{M}(\vec{\varphi}(t))\right]$ is the inertial matrix; $\left[\mathrm{C}(\vec{\varphi}(t),\dot{\vec{\varphi}}(t))\right]$ is the angular speed coupling matrix, $\left[\mathrm{P}(\vec{\varphi}(t))\right]$ is the vector that includes gravity and cable tension terms and $\vec{\tau}(t)$ is the vector of joint torques. The product $\left[\mathrm{C}(\vec{\varphi}(t),\dot{\vec{\varphi}}(t))\right]\dot{\vec{\varphi}}(t)$ represents all combined products of the joint angular speeds, which consists of the Coriolis and relative normal accelerations. The matrix $\left[\mathrm{M}(\vec{\varphi})\right]$ and vector $\left[\mathrm{C}(\vec{\varphi}(t),\dot{\vec{\varphi}}(t))\right]\dot{\vec{\varphi}}(t)$ are given in [16].

The vector of conservative generalized forces $\left[\mathrm{P}(\vec{\varphi}(t))\right]$ requires an explanation that is related to further analysis. The vector of conservative generalized forces $\left[P(\vec{\varphi})\right]$ is:

$$\left[\begin{array}{c}
m_t g(-l_{t1}s\varphi_{123}-l_{t2}c\varphi_{123})+m_{2'}g(l_1 s\varphi_{1235}+l_{c2'}s\varphi_{12356})+m_1 g l_{c1'}s\varphi_{1235} \\
\hline
k_{sl}\Delta L_l(\varphi_2,\varphi_4)\dfrac{-h_{\mathrm{AA}}c\varphi_2-h_{\mathrm{AA}}s\varphi_2}{\overline{AA'}(\varphi_2)}-m_1 g((l_1-l_{c1})s\varphi_{23}-l_{c1'}s\varphi_{1235}) \\
+k_{sr}\Delta L_r(\varphi_2,\varphi_4)\dfrac{h_{\mathrm{BB}}c\varphi_2-h_{\mathrm{BB}}s\varphi_2}{\overline{BB'}(\varphi_2)}-m_t g l_{t1}c\varphi_{123}+ \\
m_{2'}g(-l_1(s\varphi_{23}+s\varphi_{1235})-l_{c2'}s\varphi_{12356}) \\
\hline
m_t g l_{t1}c\varphi_{123}+m_1 g((l_1+l_{c1})s\varphi_{23}+l_{c1'}s\varphi_{1235})+m_{2'}g(l_1(s\varphi_{23}+s\varphi_{1235}) \\
-l_2 s\varphi_3+l_{c2'}s\varphi_{12356})-m_2 g l_{c2}s\varphi_3 \\
\hline
-m_1 g l_{c1'}s\varphi_{1235}-m_{2'}g(l_1 s\varphi_{1235}+l_{c2'}s\varphi_{12356}) \\
\hline
k_{sl}\Delta L_{lsw}(\varphi_6,\varphi_8)\dfrac{-h_{\mathrm{AA}}c\varphi_6-h_{\mathrm{AA}}s\varphi_6}{\overline{AA'}(\varphi_6)}+ \\
k_{sr}\Delta L_{rsw}(\varphi_6,\varphi_8)\dfrac{h_{\mathrm{BB}}c\varphi_6-h_{\mathrm{BB}}s\varphi_6}{\overline{BB'}(\varphi_6)}+m_{2'}g l_{c2'}s\varphi_{12356}
\end{array}\right] \tag{8}$$

where $k_{sr}$, $k_{sl}$ are the cable stiffness coefficients for the front and the back cable, and:

$$\begin{aligned}
\Delta l_r &= \Delta l_r(\varphi_2,\varphi_4)=\overline{BB'}(\varphi_2)-\overline{BB'}_0+\frac{S_{r0}}{k_{Sr}}-\int_0^{\varphi_4}R_{\mathrm{Pr}}(\theta)\,d\theta \\
\Delta l_l &= \Delta l_l(\varphi_2,\varphi_4)=\overline{AA'}(\varphi_2)-\overline{AA'}_0+\frac{S_{l0}}{k_{Sl}}+\int_0^{\varphi_4}R_{Pl}(\theta)\,d\theta \\
\Delta l_{rsw} &= \Delta l_{rsw}(\varphi_6,\varphi_8)=\overline{BB'}_{sw}(\varphi_6)-\overline{BB'}_0+\frac{S_{r0}}{k_{Sr}}-\int_0^{\varphi_8}R_{Pr}(\theta)\,d\theta \\
\Delta l_{lsw} &= \Delta l_{lsw}(\varphi_6,\varphi_8)=\overline{AA'}_{sw}(\varphi_6)-\overline{AA'}_0+\frac{S_{l0}}{k_{Sl}}+\int_0^{\varphi_8}R_{Pl}(\theta)\,d\theta
\end{aligned} \tag{9}$$

are the deformation of cable springs as functions of the knee and pulley angles. The new quantities included in (9) denote the following: $S_{r0}$ and $S_{l0}$ are the cable pre-tensions, $R_{Pr}(\theta)$ and $R_{Pl}(\theta)$ are the pulley variable radii given by (6) and $\theta$ is the geometrical angle of the cable guide on the pulley, as shown in Figure 3. The integrals in (9) represent the stored cable along the pulley thread. The vector of torques $\vec{\tau}$ in (7) is:

$$\vec{\tau}(t)=\left[\tau_{\mathrm{h}}(t)\quad\tau_{\mathrm{p}}(t)\quad\tau_{\mathrm{a}}(t)\quad\tau_{\mathrm{hsw}}(t)\quad\tau_{\mathrm{psw}}(t)\right]^T \tag{10}$$

where $\tau_{\mathrm{h}}(t)$, $\tau_{\mathrm{p}}(t)$ and $\tau_{\mathrm{a}}(t)$ are the torques at the hip, pulley and ankle joints of the stance leg. $\tau_{\mathrm{hsw}}(t)$ and $\tau_{\mathrm{psw}}(t)$ are the torques at the hip and the pulley of the swing leg.

If we consider the system shown in Figure 1, each leg would be 4-dof and matrices in (7) would be 8 x 8 and the vectors would be 8 x 1, which would increase the computational efforts in the system controller algorithm. By neglecting the pulley drive moment of inertia and neglecting the swing leg foot dynamics (the foot is considered as a point mass at the end of the swing leg), the mathematical model is reduced to five differential equations of the second order. However, we need the moment balancing equation of the pulley–cables system. The equation is:

$$-k_{\mathrm{Sr}}\Delta l_r(\varphi_2,\varphi_4)R_{Pr}(\varphi_4)+k_{\mathrm{Sl}}\Delta l_l(\varphi_2,\varphi_4)R_{Pl}(\varphi_4)=\tau_{\mathrm{p}}(t) \tag{11}$$

$$-k_{Sr}\Delta l_{rsw}(\varphi_6,\varphi_8)R_{Pr}(\varphi_8)+k_{Sl}\Delta l_{lsw}(\varphi_6,\varphi_8)R_{Plsw}(\varphi_8)=\tau_{psw}(t)$$

where $\tau_p(t)$ and $\tau_{psw}(t)$ are the torques provided by the pulley drives.

Equations (7) through (11), along with the kinematic relations, and the matrices $\left[M(\vec{\phi})\right]$ and $\left[C(\vec{\phi}(t),\dot{\vec{\phi}}(t))\right]$ given in [16] represent the walking robot mathematical model. For the purpose of controller design, the mathematical model (7) must be converted to a state-space model, i.e. a set of first order differential equations.

**2.5 State-space model**

Since the mass matrix in (7) is always invertible, the equation can be explicitly solved with respect to the angular accelerations as

$$\ddot{\vec{\varphi}}=-\left[M(\vec{\varphi})\right]^{-1}\left[C(\vec{\varphi},\dot{\vec{\varphi}})\right]\dot{\vec{\varphi}}-\left[M(\vec{\varphi})\right]^{-1}\left[P(\vec{\varphi})\right]+\left[M(\vec{\varphi})\right]^{-1}\vec{\tau}\quad\text{or}$$

$$\ddot{\vec{\varphi}}=\vec{f}(\vec{\varphi},\dot{\vec{\varphi}})+G(\vec{\varphi})\vec{\tau} \tag{12}$$

where

$$\vec{f}(\vec{\varphi},\dot{\vec{\varphi}})=-\left[M(\vec{\varphi})\right]^{-1}\left[C(\vec{\varphi},\dot{\vec{\varphi}})\right]\dot{\vec{\varphi}}-\left[M(\vec{\varphi})\right]^{-1}\left[P(\vec{\varphi})\right],\ G(\vec{\varphi})=\left[M(\vec{\varphi})\right]^{-1}$$

By assigning variables: $\xi_1=\varphi_1$, $\xi_2=\dot{\xi}_1=\dot{\varphi}_1$, $\xi_3=\varphi_2$, $\xi_4=\dot{\xi}_3=\dot{\varphi}_2$, $\xi_5=\varphi_3$, and $\xi_6=\dot{\xi}_5=\dot{\varphi}_3$, $\xi_7=\varphi_5$, $\xi_8=\dot{\xi}_7=\dot{\varphi}_5$, $\xi_9=\varphi_6$ and $\xi_{10}=\dot{\xi}_9=\dot{\varphi}_6$ the state-space model has the form:

$$\begin{bmatrix}\dot{\xi}_1\\ \dot{\xi}_2\\ \dot{\xi}_3\\ \dot{\xi}_4\\ \dot{\xi}_5\\ \dot{\xi}_6\\ \dot{\xi}_7\\ \dot{\xi}_8\\ \dot{\xi}_9\\ \dot{\xi}_{10}\end{bmatrix}=\begin{bmatrix}\xi_2\\ f_2(\vec{\xi})\\ \xi_4\\ f_4(\vec{\xi})\\ \xi_6\\ f_6(\vec{\xi})\\ \xi_7\\ f_8(\vec{\xi})\\ \xi_9\\ f_{10}(\vec{\xi})\end{bmatrix}+\begin{bmatrix}0 & 0 & \cdots & 0\\ G_{11}(\vec{\xi}) & G_{12}(\vec{\xi}) & \cdots & G_{15}(\vec{\xi})\\ 0 & 0 & \cdots & 0\\ G_{21}(\vec{\xi}) & G_{22}(\vec{\xi}) & \cdots & G_{25}(\vec{\xi})\\ 0 & 0 & \cdots & 0\\ G_{31}(\vec{\xi}) & G_{32}(\vec{\xi}) & \cdots & G_{35}(\vec{\xi})\\ 0 & 0 & \cdots & 0\\ G_{41}(\vec{\xi}) & G_{42}(\vec{\xi}) & \cdots & G_{45}(\vec{\xi})\\ 0 & 0 & \cdots & 0\\ G_{51}(\vec{\xi}) & G_{52}(\vec{\xi}) & \cdots & G_{55}(\vec{\xi})\end{bmatrix}\begin{bmatrix}\tau_h\\ \tau_p\\ \tau_a\\ \tau_{hsw}\\ \tau_{psw}\end{bmatrix} \tag{13}$$

where $f_i(\vec{\xi})$, $G_{ij}(\vec{\xi})$ ($i$ = 2,4,..,10; $j$ = 1,2,...,5) represents the entries of the functions in (12).

**2. 6 Interconnections with other supporting legs**

The interconnections with other supporting legs can be viewed as disturbances when it is not convenient to expand the mathematical model of the system and the controller complexity. However, if it is necessary to obtain better controller performance, the interconnections can be modeled as follows.

The interconnections between the supporting leg models can be interpreted through the interconnecting force and torque, as shown in Figure 2. The interconnecting force and torque can be included in the existing model through the joint torque expressions. The augmented torque vector given by (10) becomes:

$$\tau_1'=\tau_h+\tau_t+F_{tx}(l_{P1}c\varphi_{123}-l_{P2}s\varphi_{123})+F_{ty}(-l_{P1}s\varphi_{123}-l_{P2}c\varphi_{123})$$
$$\tau_2'=-\tau_t+F_{tx}(-l_1c\varphi_{23}-l_{P1}c\varphi_{123}+l_{P2}s\varphi_{123})+$$
$$F_{ty}(-l_1c\varphi_{23}-l_{P1}s\varphi_{123}+l_{P2}c\varphi_{123}) \tag{14}$$
$$\tau_3'=\tau_a+\tau_t+F_{tx}(l_2c\varphi_3+l_1c\varphi_{23}+l_{P1}c\varphi_{123}-l_{P2}s\varphi_{123})+$$
$$F_{ty}(-l_2s\varphi_3+l_1s\varphi_{23}-l_{P1}s\varphi_{123}-l_{P2}c\varphi_{123})$$
$$\tau_4'=\tau_{hsw},\ \tau_5'=\tau_{psw}$$

where the meaning of the interconnecting forces and the torques is explained earlier and shown in Figure 2, while the swing leg torques remain the same. There is influence of the interconnection forces on swing leg dynamics, through the trunk accelerations inertial effects. However, these effects are already included in the swing leg dynamics. The next section designs a controller from the dynamic model.

## 3. CONTROLLER DESIGN

The controller design for the walking robot will be based on trajectory regulation control [14].

**3.1 Controller Architecture**

The control system architecture, shown in Figure 6, consists of [14, 15]:

(a) Nominal trajectories generator,
(b) Inverse dynamics for nominal control calculation,
(c) Tracking error regulation controller,
(d) Measurement system, and
(e) Plant

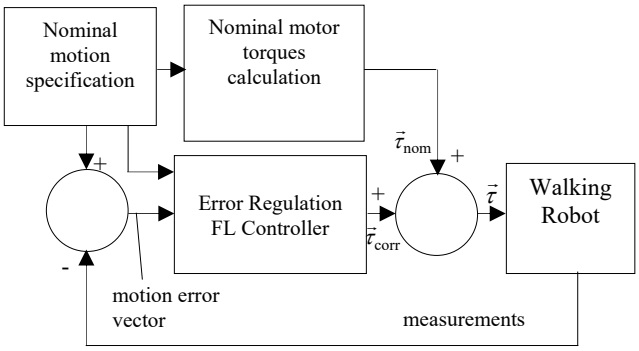


**Figure 6. The trajectory regulation controller architecture**

The nominal motion specification block generates the joint trajectories that will provide a balanced walk. The nominal joint angles at every time step is sent to the error dynamics controller and the nominal torques generator. The nominal torques are generated based on the inverse dynamics mathematical model. Since the robot mathematical model is not an exact dynamic description, there will be errors in the resulting motion. The amount of the resulting motion deviation from the desired motion is calculated based on the measurements of the joint angles which is used by the error dynamics controller to generate correction torques.

The inverse dynamics that is used to generate the nominal torques is obtained directly from (7), where the torques are explicitly expressed in terms of the functions of angles and their first two derivatives. However, the derivatives of the input signals must be obtained in the Laplace domain via pseudo-differentiators of the form:

$$\Phi(s)=\frac{s}{\varepsilon s+1}\qquad\qquad \varepsilon\in\left[10^{-3},10^{-2}\right]$$

to obtain physically-realizable derivatives. Since the controller architecture is based on error dynamics, we need to obtain the appropriate error dynamics model.

### 3.2 Error dynamics

The error dynamics model is based on the state-space model (13):

$$\begin{bmatrix} \dot{\tilde{\xi}}_1 \\ \dot{\tilde{\xi}}_2 \\ \dot{\tilde{\xi}}_3 \\ \dot{\tilde{\xi}}_4 \\ \dot{\tilde{\xi}}_5 \\ \dot{\tilde{\xi}}_6 \\ \dot{\tilde{\xi}}_7 \\ \dot{\tilde{\xi}}_8 \\ \dot{\tilde{\xi}}_9 \\ \dot{\tilde{\xi}}_{10} \end{bmatrix} = \begin{bmatrix} \tilde{\xi}_2 \\ f_2(\vec{\xi}) - f_2(\vec{\bar{\xi}}) \\ \tilde{\xi}_4 \\ f_4(\vec{\xi}) - f_4(\vec{\bar{\xi}}) \\ \tilde{\xi}_6 \\ f_6(\vec{\xi}) - f_6(\vec{\bar{\xi}}) \\ \tilde{\xi}_8 \\ f_8(\vec{\xi}) - f_8(\vec{\bar{\xi}}) \\ \tilde{\xi}_{10} \\ f_{10}(\vec{\xi}) - f_{10}(\vec{\bar{\xi}}) \end{bmatrix} + \begin{bmatrix} 0 & 0 & \cdots & 0 \\ G_{11}(\vec{\bar{\xi}}) & G_{12}(\vec{\bar{\xi}}) & \cdots & G_{15}(\vec{\bar{\xi}}) \\ 0 & 0 & \cdots & 0 \\ G_{21}(\vec{\bar{\xi}}) & G_{22}(\vec{\bar{\xi}}) & \cdots & G_{25}(\vec{\bar{\xi}}) \\ 0 & 0 & \cdots & 0 \\ G_{31}(\vec{\bar{\xi}}) & G_{32}(\vec{\bar{\xi}}) & \cdots & G_{35}(\vec{\bar{\xi}}) \\ 0 & 0 & \cdots & 0 \\ G_{41}(\vec{\bar{\xi}}) & G_{42}(\vec{\bar{\xi}}) & \cdots & G_{45}(\vec{\bar{\xi}}) \\ 0 & 0 & \cdots & 0 \\ G_{51}(\vec{\bar{\xi}}) & G_{52}(\vec{\bar{\xi}}) & \cdots & G_{55}(\vec{\bar{\xi}}) \end{bmatrix} \begin{bmatrix} \tilde{\tau}_{\mathrm{h}} \\ \tilde{\tau}_{\mathrm{p}} \\ \tilde{\tau}_{\mathrm{a}} \\ \tilde{\tau}_{\mathrm{hsw}} \\ \tilde{\tau}_{\mathrm{psw}} \end{bmatrix} \tag{15}$$

where $\vec{\bar{\xi}}$ denotes the nominal trajectory of the system state (angles and angular velocities) in the state-space, $\tilde{\xi}_i = \xi_i - \bar{\xi}_i$ is the error of the $i$-th variable with respect to its nominal value for the specified time and $\tilde{\tau}_j$ ($j \in$ {h,p,a,hsw,psw}) represents corrective torque inputs, generated by the feedback controller with the objective to exponentially satisfy $\left\| \vec{\tilde{\xi}} \right\| \to 0$. Error vector is stabilization is discussed in the following.

### 3.3 Control Law

The control law should provide the corrective torques such that the errors exponentially converge to zero. To achieve this goal, the control inputs cancel the nonlinearity (feedback linearization) and introduce the terms proportional to the errors of the states as follows.

$$\begin{aligned} G_{11}\tau_h + G_{12}\tau_p + G_{13}\tau_a + G_{14}\tau_{hsw} + G_{15}\tau_{psw} &= \tilde{b}_{g1} \\ G_{21}\tau_h + G_{22}\tau_p + G_{23}\tau_a + G_{24}\tau_{hsw} + G_{25}\tau_{psw} &= \tilde{b}_{g2} \\ G_{31}\tau_h + G_{32}\tau_p + G_{33}\tau_a + G_{34}\tau_{hsw} + G_{35}\tau_{psw} &= \tilde{b}_{g3} \\ G_{41}\tau_h + G_{42}\tau_p + G_{43}\tau_a + G_{44}\tau_{hsw} + G_{45}\tau_{psw} &= \tilde{b}_{g4} \\ G_{51}\tau_h + G_{52}\tau_p + G_{53}\tau_a + G_{54}\tau_{hsw} + G_{55}\tau_{psw} &= \tilde{b}_{g5} \end{aligned} \tag{16}$$

where

$$\begin{aligned} \tilde{b}_{g1} &= -f_2(\vec{\xi}) + f_2(\vec{\bar{\xi}}) - k_{21}\tilde{\xi}_1 - k_{22}\tilde{\xi}_2 \\ \tilde{b}_{g2} &= -f_4(\vec{\xi}) + f_4(\vec{\bar{\xi}}) - k_{43}\tilde{\xi}_3 - k_{44}\tilde{\xi}_4 \\ \tilde{b}_{g3} &= -f_6(\vec{\xi}) + f_6(\vec{\bar{\xi}}) - k_{65}\tilde{\xi}_5 - k_{66}\tilde{\xi}_6 \\ \tilde{b}_{g4} &= -f_8(\vec{\xi}) + f_8(\vec{\bar{\xi}}) - k_{87}\tilde{\xi}_7 - k_{88}\tilde{\xi}_8 \\ \tilde{b}_{g5} &= -f_{10}(\vec{\xi}) + f_{10}(\vec{\bar{\xi}}) - k_{109}\tilde{\xi}_9 - k_{1010}\tilde{\xi}_{10} \end{aligned}$$

and $k_{ij}$ ($i$ = 2,4,...,10; $j$ = $i$-1,$i$) are constants to be determined, such that the closed control loop error dynamics are exponentially stable and have desired transient behavior.

We specify overshoot less than 5%, and settling time less than 0.5 seconds for each joint, which results in the damping coefficient $\zeta > 0.69$ and the natural frequency $\omega_n > 11.59 \frac{\text{rad}}{\text{s}}$. To obtain these two values, the coefficients $k_{ij}$ need to have the following values:

$$k_{i,i-1} = 134.3 \left(\frac{\text{rad}}{\text{s}}\right)^2, \; k_{ii} = 16 \left(\frac{\text{rad}}{\text{s}}\right), \; (i = 2,4,...,10)$$

The control law is:

$$\vec{\tilde{\tau}} = G^{-1}\vec{\tilde{b}}_g \tag{17}$$

Where $G$ is the reduced input matrix in (15) (without zero rows) evaluated at the nominal trajectory $\vec{\bar{\xi}}$. Next, we will evaluate the performance of the control law via simulations.

### 3.4 Simulation Results and the Performance Analysis

The block diagram shown in Figure 6 is implemented in MATLAB/Simulink; the control law is tested on a combination of ramp inputs for the joints angles and the simulation results are shown in the following figures.

The nominal joint angles and the smooth pseudo-differentiator-obtained angular velocity trajectories are shown in Figure 7 and nominal torques predicted by the inverse dynamics block are shown in Figure 8. The results in the nominal torques plot agree with the expected results since the moment arm is significantly greater for the knee joint than for the other two joints. The hip joint has low predicted torque due to the fact that the CG of the trunk for the prescribed motion is vertically above the hip.

Cable tensions to provide the knee joint angular trajectory are shown in Figure 9. The plot shows that the cables pre-tension was 50 N and could have been reduced more and still avoid a slack cable case.

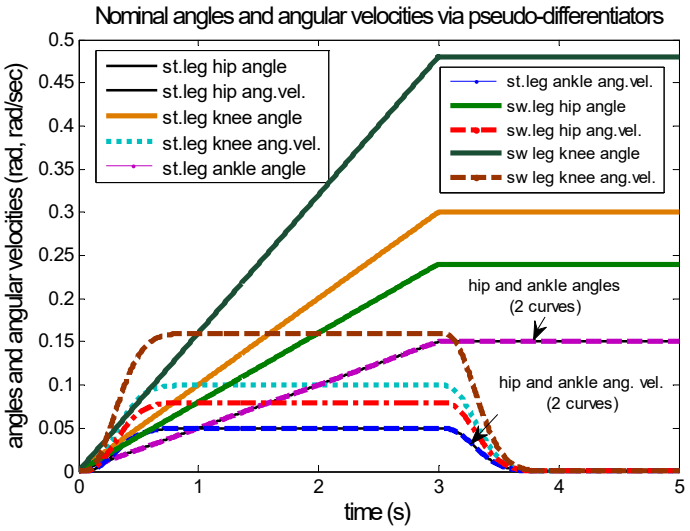


**Figure 7. Nominal walking state trajectories**

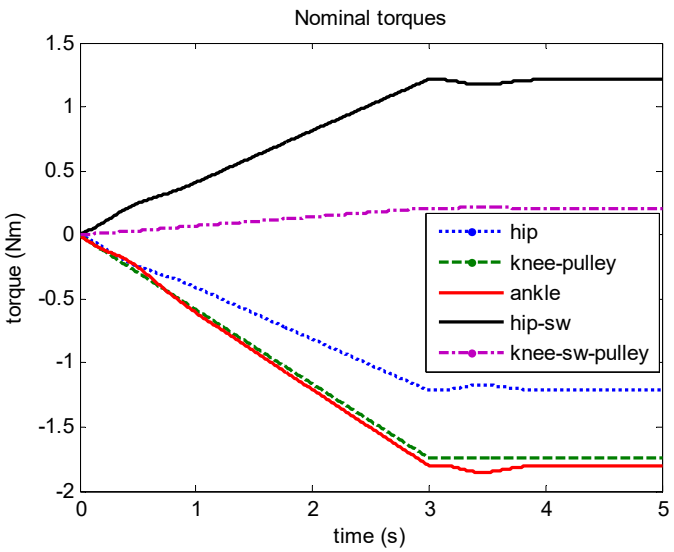


**Figure 8. Nominal joint torques**

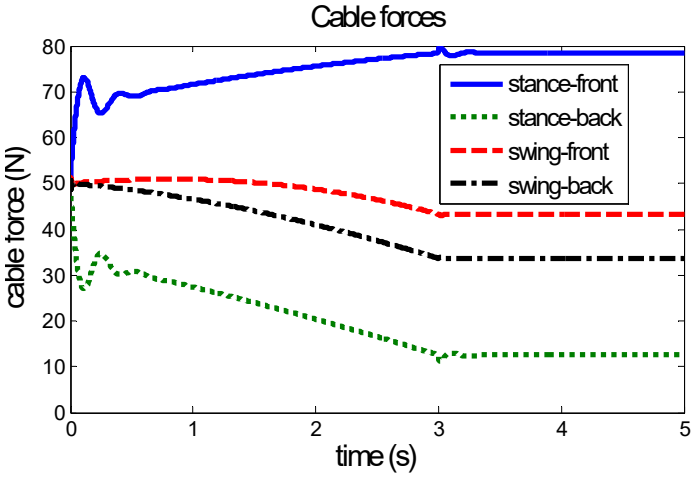


**Figure 9. Cable forces (tensions)**

The comparison of the actual vs. the desired angles is shown in Figure 10. The plot shows very low errors of the actual trajectories (the ankle and the hip have the same nominal trajectory in the plot). Deviation is noticeable at the instants when there are sharp changes in the desired trajectory slope. The small deviation of the actual from the desired angles can be seen in the errors plot, Figure 11.

Total robot joint torques are shown in Figure 12. If the nominal torques, shown in Figure 8, are compared with the total torques, significant corrective torque values can be noticed at the instants when there is significant change in the desired speed of the joints, due to the inertial effects and the effect of the pseudo-differentiation. The total torques consist of the nominal torques shown in Figure 8 and the corrective torques shown in Figure 13. The reason that the corrective torques do not approach zero in a steady state condition is that the controller is tested on a regular perturbation by changing the position of the trunk CG for 0.05 m (horizontally). However, the actual trajectories of the joint angles still approach the nominal trajectories with satisfactory dynamics and error limits.

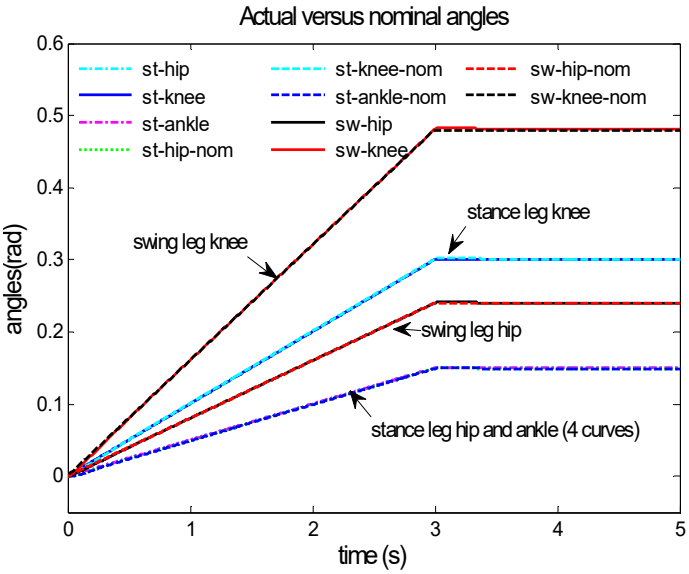


**Figure 10. The actual versus desired trajectories**

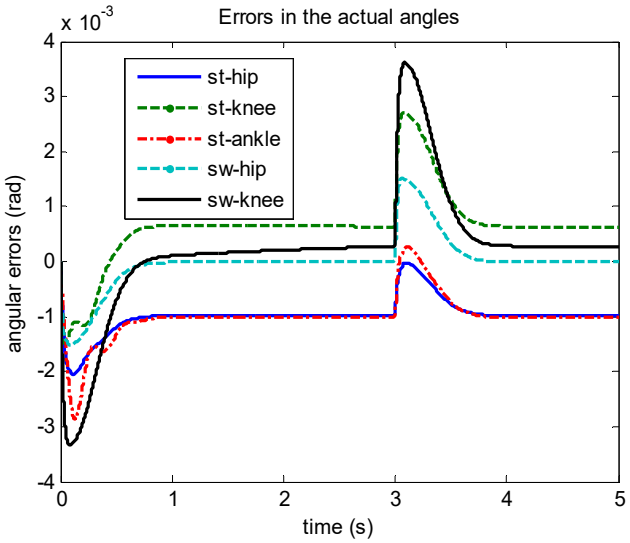


**Figure 11. Hip, knee and ankle joint angle errors for the stance leg**

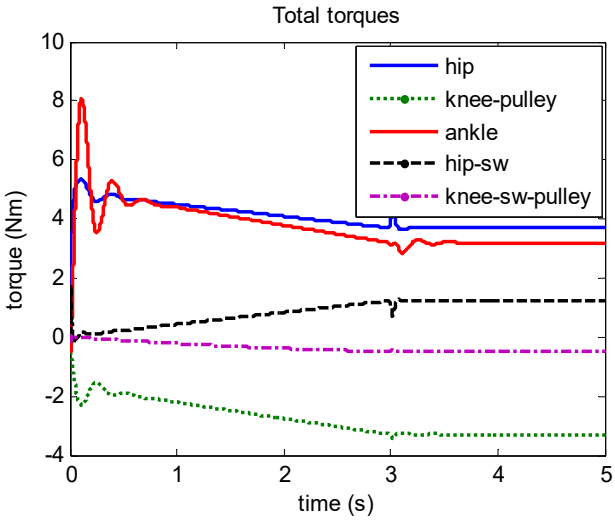


**Figure 12. Total joint torques**

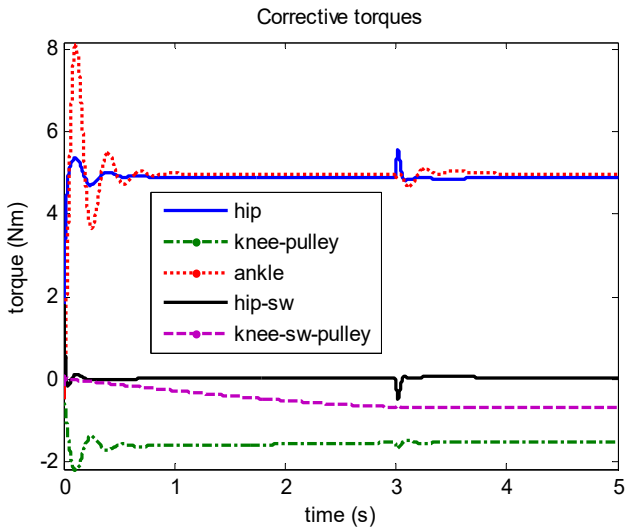


**Figure 13. Corrective torques signals generated by the controller**

## 4. CONCLUSION

This article presented a walking robot actuation system based on a combination of direct-drive actuation and elastic-cable actuation. Several benefits are introduced using the cables to actuate joints. Energy consumption is reduced through the reduction of the inertial forces on most mobile robot parts. A threaded pulley profile with the variable radius is introduced to ensure that, along with relatively small deformations of the cable spring, the cables do not become loose, which would lead directly into complications with pure transport delays in the control law.

The mathematical model is derived, with respect to the assumptions that are listed. The stance leg – swing leg – trunk dynamics model is presented in state-space form and the corresponding error dynamics is used to design the controller using trajectory regulation control with an open-loop nominal controller and a closed-loop tracking error regulation controller. The nominal controller is based on the inverse dynamics model of the plant. The closed-loop controller is based on feedback linearization control, where plant nonlinearity is cancelled by state feedback, and desired linear dynamics are assigned. It is shown how the model can be combined through the interconnection quantities with another leg-trunk model to consider the dynamic impact from the other supporting legs.

The performance of the joint trajectories tracking was analyzed using simulations, which showed satisfactory results of tracking the prescribed joint trajectories. Possible problematic cases in tracking include cases with sharp changes and/or associated noise in the desired trajectories, due to the need of finding approximate derivatives.

## ACKNOWLEDGMENT

We thank Mr. Justin Mamrak, a Ph.D. student in the School of Electrical Engineering and Computer Science at Ohio University, for assistance in assembling the RoboCat hardware.

## REFERENCES

[1] G.A. Cavagna, N.C. Heglund, and C.R. Taylor, “Mechanical work in terrestrial locomotion: two basic mechanisms for minimizing energy expenditure”, *Am J Physiol.*; 233**,** 1977.

[2] B.R. Umberger and P.E. Martin, “Mechanical power and efficiency of level walking with different stride rates”, *The Journal of Experimental Biology,* 210: 3255-326, 2007.

[3] A. Ruina, J.E. Bertram, and M. Srinivasan, “A collisional model of the energetic cost of support work qualitatively explains leg sequencing in walking and galloping, pseudo-elastic leg behavior in running and the walk-to-run transition”, *Journal of Theoretical Biology*, 237: 170–192, 2005.

[4] world.honda.com/ASIMO, accessed 7/1/2014.

[5] www.takanishi.mech.waseda.ac.jp/top/research/wabian, accessed 7/16/2014.

[6] B. Vanderborght, R. Van Ham, B. Verrelst, M. Van Damme, D. Lefeber, “Overview of the Lucy Project: Dynamic Stabilization of a Biped Powered by Pneumatic Artificial Muscles,” *Advanced Robotics*, 22: 1027–1051, 2008.

[7] www.humanoid.waseda.ac.jp/booklet/kato_4.html, accessed 7/23/2014.

[8] A.E. Aliev, “Giant-Stroke, Superelastic Carbon Nanotube Aerogel Muscles”, *Science*, 323: 1575-1578, 2009.

[9] R.H. Baughman, “Playing Nature's Game with Artificial Muscles,” *Science*, 308: 63-65, 2005.

[10] Y. Bar-Cohen and S. Leary, “Electroactive Polymers as Artificial Muscles changing Robotics Paradigms”, National Space and Missile Materials Symposium, 2000.

[11] E. Kljuno and R.L. Williams II, “Vehicle Simulation System: Controls and Virtual-Reality-Based Dynamics Simulation”, *Journal of Intelligent and Robotic Systems*, 52: 79-99, 2008.

[12] A.P. Bowling, “Mass Distribution Effects on Dynamic Performance of a Cable-Driven Hexapod,” *ASME Journal of Mechanical Design*, 129(8); 887-890, 2007.

[13] E. Kljuno, J.J. Zhu, R.L. Williams II and S.M. Reilly, “A Biomimetic Elastic Cable-driven Quadruped Walking Robot – RoboCat”, *ASME*, IMECE, 2011.

[14] H.K. Khalil, Nonlinear Systems, Second Edition, Englewood Cliffs, NJ, Prentice-Hall, 1996.

[15] J.J. Zhu, “Lecture Notes on Nonlinear Systems Control: Blue Book,” Ohio University, 2008.

[16] E. Kljuno, 2012, “Elastic Cable-Driven Bipedal Walking Robots: Design, Modeling, Dynamics and Controls”, Ph.D. Dissertation, Mechanical Engineering, Ohio University.